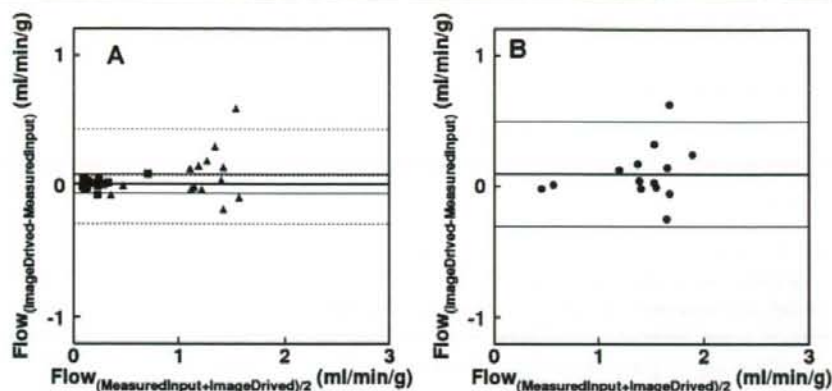**Fig. 9** **a** Bland–Altman plot for arterial (*square*), portal (*triangle*) and **b** total hepatic blood flow differences between measured and image-derived input functions


degree of overlap and tight correlations were observed between the estimated input functions and those obtained during online blood sampling/counting. Consequently, calculated flow values were consistent between the methods. Alternative to the present procedure, a ROI-based input extraction from PET images has been used for the carotid artery in [11C]flumazenil brain studies [27], abdominal artery for kidney blood flow quantification with $H_2^{15}O$ [15], and aorta for cardiac 18F-FDG metabolism [32], and for tumor blood using $H_2^{15}O$ [34]. In these approaches, ROIs are drawn in visible vessels, and the partial volume effect must be taken into account by testing different ROI sizes or by thresholding the pixels inside arterial ROIs; the need for partial volume correction remains a necessary limitation. Closer to the current analysis, Edward et al. applied multiple tissue curves to estimate quantitative kinetic parameters in the brain [7] and well reproduced the input function for H_{15}^2O. However, their formula did not take into account the radioactivity from the blood component inside the tissue ROI, and the validity of their method may not be directly extrapolated to the liver because of the large proportion of blood, which is typically ranging between 0.27 and 0.40 ml/ml [23] in this organ.

The present method showed that the height of the estimated input is almost doubled if the blood volume is not included in the formula and if the arterial volume contributes 10% of radioactivity in the tissue TACs in our preliminary study (data not shown). The shape of an arterial input function from multiple tissue TACs has been well reproduced in brain 18FDG or [11C]MPDX studies by using an independent component analysis-based method (extraction of the plasma TAC using independent component analysis [24, 25] still requiring one arterial blood sample, and the combination of the latter and the current techniques may be of further simplification and deserves investigation since it would entail neither a model function nor direct blood measurements.

One advantage of introducing a model function was to shape the model input function by imposing constrains to the parameters range, allowing to overcome noise problems caused by limited scan duration and short half-life of 15O. The present approach may be applicable to a study group including subjects with hepatic disorders as far as measurement conditions are equivalent and the shape of the input function can be expected to be similar, though the validity of the present method was tested in normal animals. We

Fig. 10 **a** Bland–Altman plot for arterial (*square*), portal (*triangle*), and **b** total hepatic blood flow differences between ultrasonography and kinetic modeling using image-derived input functions
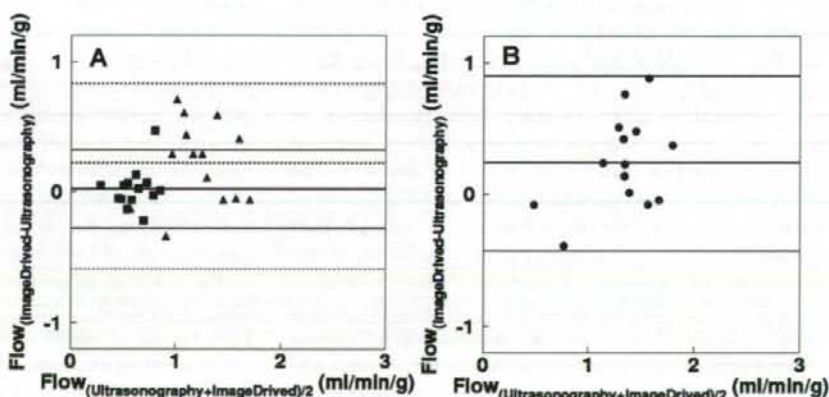
expect no relevant limitation in the extension of the assumptions concerning the shape to other species and in a majority of hepatic conditions. A drawback in the use of a model function, however, is that the feasibility is unknown for a group in which the shape of input functions could be extremely different or cannot be expressed by the present model function. This is not a commonly expected case. In this situation, the present method would require to, and may still be adapted, by introducing group-specific parameter constraints or a modified model function. The present model function was created by assuming the model, namely, tracer bidirectional diffusion to whole body as in differential Eq. 9. The solution was derived as Eq. 10, and the model function was modified to avoid the one order term of t, which would complicate calculations in the following procedures, i.e., model function for portal input and for tissue response functions. This modification could deteriorate the physiological mean of parameters, such as K_e and K_i; however, the input functions obtained in the present study using this modified equation well reproduced the shape of measured inputs. The modified model function and derived portal model function seemed to be superimposable to measured blood TACs, although there were slight, few-second systematic misalignments in the peak of arterial blood and overestimations at the late phase. This suggested that the error in the position of the peak and in late phase in the estimated input function against measured ones (Figs. 7 and 8) is due to a limitation in the description of the model function.

The present estimation procedure followed two steps, as designed to fit tissue curves individually, and then simultaneously. The first step allowed careful exclusion of tissue TACs showing t_1 or t_2 values over one standard deviation from the mean to eliminate the influence of radioactivity outside the liver region. In fact, in the experimental procedure, $H_2^{15}O$ was injected in the femoral vein, draining into the vena cava, which is not distant from the liver. Other adjacent high-perfusion organs include the kidneys. The influence of ROIs drawn in proximity of these regions was not included in the model. Thus, special attention was paid at excluding confounding tissue TACs by examining t_1 and t_2. In the above examples, the tracer was expected to show an early peak in case of an anatomical overlap with the vena cava, and the extracted TAC covering this region was omitted in this step. The second step was introduced to facilitate the achievement of the convergence by fixing the values of t_1, t_2, and r_a to their calculated means (as obtained above) to estimate the remaining two parameters. Generally, if many parameters are estimated in a fitting procedure such as in the present method, there could be many local minima, and uniqueness of parameter solution might not be guaranteed. As shown in the simulation study, the three parameters t_1, t_2, and r_a were

estimated independent of the number of tissue TACs; however, the remaining two parameters A and $K_e(1+\alpha)$ were dependent on that. This suggests that correlation among parameters due to their numerosity could not be prevented. However, the shapes of input functions were reproduced, and flow values were consistent with other two methods, i.e., those computed from measured inputs and from ultrasonography. Thus, the correlation among parameters did not seem to affect the estimation of flow values, although further study is required for optimization.

We used a fixed value of k_g to represent the diffusion rate of water between arterial blood and the gut compartment in the estimation of the portal input. The deviation in this rate constant was about 26% in the current study group. The simulation analysis showed that values within 20% of the assumed true k_g number corresponded to a propagated error of 10% in the final estimation of hepatic perfusion. The value of k_g used in our final computations is in accordance with the recently reviewed concept that [20] in mammals, the general biological rate (uptake ratio) varies approximately in proportion to the 3/4 power of body size and, given a body mass of ~60 kg, k_g, which is the uptake rate of water in the gut system, can be predicted to fall around 0.45 min^{-1} in humans. This number is consistent with a mean figure of 0.5 min^{-1}, as obtained in this study, suggesting that the present assumption could be implemented to obtain the liver input function in humans. We also assumed a time delay of portal input to be zero against the arterial one. The deviation in this time was about 0.7 s in the current study group. The simulation analysis showed that an error in this value within 10 s corresponded to a propagated error of less than 10% in the final estimation of hepatic perfusion. Of further strength, a close agreement was shown between estimated and measured blood activity curves and estimated and Doppler-determined liver flow results. The larger difference of the latter result against the former result might be due to the model assumptions in flow calculations, as well as in the assumption of circular shape when estimating the area of the arterial and portal vessels by ultrasonography and in the accuracy of ultrasonography data (from multiple measurements of flow data, coefficient of variation was 13±5% for portal flow and 18± 10% for hepatic arterial flow with this study [data not shown]). In this study, the flow values were calculated assuming the dual input, single compartment model [2, 29, 30, 35]. Altogether, the above observations support the use of a fixed k_g and the current model in the fully non-invasive quantification of liver perfusion.

The validation of the current approach, as obtained in this study, is especially valuable in the liver for multiple reasons. First, the inaccessibility of the portal vein prevents its direct blood sampling in humans. Arterial blood can be obtained [8, 9, 16, 17, 26, 33], but blood counting requires corrections for

dispersion, delay between target organ and sampling device, and cross calibration between PET scanner and radioactivity counter, which are all potential sources of errors, in the same magnitude as that expected with the current method. Second, liver perfusion can be compromised both as consequence and cause of hepatic disease and is considered a prognostic indicator and useful marker during progression or treatment follow-up [6, 22]. Third, the possibility to distinctly quantify portal and arterial perfusion is important because their reciprocal compensation may be masked once only if total hepatic flow is measured.

The present simulation study allowed to establish that the optimal number of tissue TACs for DIF estimation was 10 to 20, independent of the noise levels, among the ones selected in this investigation. As pointed out by Edward et al. [7], as the noise on tissue TACs increased, the standard deviation of uptake ratio of tracer increased. Also, they suggested that the standard deviation tended to decrease when more regions were used. The present study intended to investigate the optimal number of tissue TACs from the whole region of liver. The noise in the liver can be minimized by placing a ROI to cover the whole organ and subsequently dividing it in a number of sub-regions corresponding to 10–20 under the conditions of the current experiments. The present results may depend on the reconstruction method. However, as far as the PET image is calculated quantitatively and the distribution of flow values in the extracted TACs is in the same order of magnitude as the present study, the results of optimization in this study would be applicable because those two conditions were assumed in the present simulation study. We assumed that the ratio of blood flow between the hepatic artery and the portal vein was uniform in the whole organ, as supported by an extended literature on the healthy liver and on a majority of metabolic disorders involving the organ. Conversely, the quantification of flow in hepatic tumors in which perfusion from arterial blood is predominant may be best approximated by simplifying the procedure to a single input or by fitting the relative vascular (arterial and portal) contributions as additional parameters in the model. The current procedure was validated for the determination of liver perfusion with $H_2^{15}O$ PET data. Required conditions were a model function to describe the input function and a kinetic model for tracer exchange between blood and tissue. In theory, the present method might be adapted to other tracers and organs if tracer kinetics in the tissue can be described with a model function.

In conclusion, our results demonstrate that arterial and portal vein concentrations of labeled water can be estimated directly from tissue time–activity curves obtained through dynamic $H_2^{15}O$ PET imaging. The calculated hepatic arterial, portal, and total perfusion values using estimated or measured input functions were similar and consistent with ultrasonography measurements.

Appendix

A model function for AIF was created by assuming a two-compartment model in which the tracer is administered in a rectangular form and diffuses bi-directionally between arterial and interstitial space in whole body peripheral tissue compartments. Differential equations for the model function ($C_A(t)$) can be expressed as

$$\frac{dC_A(t)}{dt} = \frac{dF}{dt} - K_e C_A(t) + K_i C_{WB}(t) \tag{9}$$

$$\frac{dC_{WB}(t)}{dt} = K_e C_A(t) - K_i C_{WB}(t) \tag{10}$$

$$\frac{dF}{dt} = A \ (t_1 \le t \le t_2) \atop 0 \ (\text{elsewhere}) \tag{11}$$

where t_1 and t_2 assumes the appearance time of administered tracer, and t_2-t_1 represents the administration duration; A corresponds to the given amount of tracer. The equation F (Eq. 11) represents the bolus administration of tracer in the rectangular form with duration t_2-t_1. $C_{WB}(t)$ is the expected tracer concentration in interstitial spaces in whole body peripheral tissues; K_e and K_i are bidirectional tracer diffusion rates between blood and peripheral tissue compartments, respectively. Solving Eq. 10 for C_{WB} gives

$$C_{WB}(t) = K_e e^{-K_i t} \int_0^t C_A(\tau) e^{K_i \tau} d\tau. \tag{12}$$

Sum of Eqs. 9 and 10 is

$$\frac{d(C_A(t) + C_{WB}(t))}{dt} = \frac{dF}{dt} \tag{13}$$

Thus,

$$C_A(t) + C_{WB}(t) = F \atop {\begin{aligned} &= 0 &(t < t_1) \\ &= A(t - t_1) &(t_1 \le t \le t_2) \\ &= A(t_2 - t_1) &(t > t_2) \end{aligned}} \tag{14}$$

Substitution of C_{WB} from Eq. 12 into 14 after multiplying $e^{K_i \cdot t}$ gives

$$e^{K_i \cdot t} C_A(t) + K_e \int_0^t C_A(\tau) e^{K_i \cdot \tau} d\tau = e^{K_i \cdot t} F \tag{15}$$

Differentiation with respect to t after arranging gives

$$\frac{dC_A(t)}{dt} = \alpha F + \frac{1}{K_e} \frac{dF}{dt} - K_e(1 + \alpha) C_A(t) \tag{16}$$

where $\alpha = K_i/K_e$. Thus,

$$C_A(t) = K_e e^{-K_e \cdot (1+\alpha) \cdot t} \int_0^t \left(\alpha F + \frac{1}{K_e} \frac{dF}{dt} \right) e^{K_e \cdot (1+\alpha) \cdot \tau} d\tau \tag{17}$$

Solving Eq. 17, we obtain

$$
\begin{aligned}
C_A(t) &= 0 & (t < t_1) \\
&= \frac{A}{K_e^2(1+\alpha)^2} \left(K_e \alpha (1+\alpha)(t - t_1) + 1 - e^{K_e \cdot (1+\alpha) \cdot (t_1 - t)} \right) & (t_1 \leq t \leq t_2) \\
&= \frac{A}{K_e^2(1+\alpha)^2} \left(K_e \alpha (1+\alpha)(t_2 - t_1) + e^{K_e \cdot (1+\alpha) \cdot (t_2 - t)} - e^{K_e \cdot (1+\alpha) \cdot (t_1 - t)} \right) & (t > t_2)
\end{aligned} \tag{18}
$$

The first term in the second equation for $t_1 < t < t_2$, i.e., $K_e \alpha (1+\alpha)(t_1 - t_2)$, would complicate further calculations (such as tissue response and portal input); thus, this term was omitted, and the model function (Eq. 18) was modified to set the C_A value as 0 at $t = t_1$, as continuous at $t = t_2$, and as non-zero value at the equilibrium, i.e., at $t = \infty$. Thus, the following equation was derived:

$$
\begin{aligned}
C_A(t) &= 0. & (t < t_1) \\
&= \frac{A}{K_e^2(1+\alpha)^2} (1 - \exp(K_e(1+\alpha)(t_1 - t))) & (t_1 \leq t \leq t_2) \\
&= \frac{A}{K_e^2(1+\alpha)^2} (\exp(K_e(1+\alpha)(t_1 - t_2)) + \exp(K_e(1+\alpha)(t_2 - t)) - 2 \cdot \exp(K_e(1+\alpha)(t_1 - t))) & (t > t_2)
\end{aligned} \tag{19}
$$

References

1. Alenius S, Ruotsalainen U. Bayesian image reconstruction for emission tomography based on median root prior. Eur J Nucl Med. 1997;24:258–65.
2. Becker GA, Muller-Schauenburg W, Spilker ME, Machulla HJ, Piert M. A priori identifiability of a one-compartment model with two input functions for liver blood flow measurements. Phys Med Biol. 2005;50:1393–404.
3. Bland JM, Altman DG. Statistical methods for assessing agreement between two methods of clinical measurement. Lancet. 1986;1:307–10.
4. Blomley MJ, Coulden R, Dawson P, et al. Liver perfusion studied with ultrafast CT. J Comput Assist Tomogr. 1995;19:424–33.
5. Carson RE. Parameter estimation in positron emission tomography. In: Phelps ME, Mazziotta JC, Schelbert HR, editors. Positron emission tomography and autoradiography: principles and applications for the brain and heart. New York, NY: Raven; 1986. p. 347–90.
6. Johnson DJ, Muhlbacher F, Wilmore DW. Measurement of hepatic blood flow. J Surg Res. 1985;39:470–81.
7. Edward VR, Di Bella EV, Clackdoyle R, Gullberg GT. Blind estimation of compartmental model parameters. Phys Med Biol. 1999;44:765–80.
8. Eriksson L, Holte S, Bohm Chr, Kesselberg M, Hovander B. Automated blood sampling system for positron emission tomography. IEEE Trans Nucl Sci. 1988;35:703–7.
9. Eriksson L, Kanno I. Blood sampling devices and measurements. Med Prog Technol. 1991;17:249–57.
10. Henderson JM, Gilmore GT, Mackay GJ, Galloway JR, Dodson TF, Kutner MH. Hemodynamics during liver transplantation: the interactions between cardiac output and portal venous and hepatic arterial flows. Hepatology. 1992;16:715–8.
11. Iida H, Kanno I, Miura S, Murakami M, Takahashi K, Uemura K. Error analysis of a quantitative cerebral blood flow measurement using $H_2^{15}O$ autoradiography and positron emission tomography, with respect to the dispersion of the input function. J Cereb Blood Flow Metab. 1986;6:536–45.
12. Iida H, Higano S, Tomura N, Shishido F, Kanno I, Miura S, et al. Evaluation of regional differences of tracer appearance time in cerebral tissues using $[^{15}O]$ water and dynamic positron emission tomography. J Cereb Blood Flow Metab. 1988;8:285–8.
13. Iozzo P, Gastaldelli A, Järvisalo MJ, Kiss J, Borra R, Buzzigoli E, et al. 18F-FDG assessment of glucose disposal and production rates during fasting and insulin stimulation: a validation study. J Nucl Med. 2006;47:1016–22.

14. Iozzo P, Järvisalo MJ, Kiss J, Borra R, Naum GA, Viljanen A, et al. Quantification of liver glucose metabolism by positron emission tomography: validation study in pigs. Gastroenterology. 2007;132:531–42.

15. Juillard L, Janier M, Fouque D, et al. Renal blood flow measurement by positron emission tomography using ^{15}O-labeled water. Kidney Int. 2000;57:2511–8.

16. Kanno I, Iida H, Miura S, Murakami M, Takahashi K, Sasaki H, et al. A system for cerebral blood flow measurement using an $H_2^{15}O$ autoradiographic method and positron emission tomography. J Cereb Blood Flow Metab. 1987;7:143–53.

17. Kudomi N, Choi E, Watabe H, Kim KM, Shidahara M, Ogawa M, et al. Development of a GSO detector assembly for a continuous blood sampling system. IEEE TNS. 2003;50:70–3.

18. Kudomi N, Watabe H, Hayashi T, Iida H. Non-invasive estimation of arterial input function for water and oxygen from PET dynamic images. J Nucl Med. 2006;47(Supplement 1):361.

19. Leen E, Goldberg JA, Anderson JR, et al. Hepatic perfusion changes in patients with liver metastases: comparison with those patients with cirrhosis. Gut. 1993;34:554–7.

20. Lindstedt, Schaeffer. Use of allometry in predicting anatomical and physiological parameters of mammals. Laboratory Anim. 2002;36:1–19.

21. Martin-Comin J, Mora J, Figueras J, et al. Calculation of portal contribution to hepatic blood flow with 99m-Tc-microcolloids. A noninvasive method to diagnose liver graft rejection. J Nucl Med. 1988;29:1776–80.

22. Materne R, Van Beers BE, Smith AM, Leconte I, Jamart J, Dehoux JP, et al. Non-invasive quantification of liver perfusion with dynamic computed tomography and a dual-input one-compartmental model. Clin Sci (Lond). 2000;99:517–25.

23. Munk OL, Bass L, Roelsgaard K, Bender D, Hansen SB, Keiding S. Liver kinetics of glucose analogs measured in pigs by PET: importance of dual-input blood sampling. Nucl Med. 2001;42:795–801.

24. Naganawa M, Kimura Y, Nariai T, et al. Omission of serial arterial blood sampling in neuroreceptor imaging with independent component analysis. NeuroImage. 2005a;26:885–90.

25. Naganawa M, Kimura Y, Ishii K, Oda K, Ishiwata K, Matani A. Extraction of a plasma time–activity curve from dynamic brain pet images based on independent component analysis. IEEE Trans on Bio-Med Eng. 2005b;52:201–10.

26. Ruotsalainen U, Raitakari M, Nuutila P, Oikonen V, Sipilä H, Teräs M, et al. Quantitative blood flow measurement of skeletal muscle using oxygen-15-water and PET. J Nucl Med. 1997;38:314–9.

27. Sanabria-Bohorquez SM, Maes A, Dupont P, Bormans G, de Groot T, Coimbra A, et al. Image-derived input function for [^{11}C] flumazenil kinetic analysis in human brain. Mol Img Biol. 2003;5:72–8.

28. Taniguchi H, Oguro A, Takeuchi K, Miyata K, Takahashi T, Inaba T, et al. Difference in regional hepatic blood flow in liver segments—non-invasive measurement of regional hepatic arterial and portal blood flow in human by positron emission tomography with H2(15)O. Ann Nucl Med. 1993;7:141–5.

29. Taniguchi H, Oguro A, Koyama H, Masuyama M, Takahashi T. Analysis of models for quantification of arterial and portal blood flow in the human liver using PET. J Comput Assist Tomogr. 1996a;20:135–44.

30. Taniguchi H, Koyama H, Masuyama M, Takada A, Mugitani T, Tanaka H, et al. Angiotensin-II-induced hypertension chemotherapy: evaluation of hepatic blood flow with oxygen-15 PET. J Nucl Med. 1996b;37:1522–3.

31. Taniguchi H, Yamaguchi A, Kunishima S, Koh T, Masuyama M, Koyama H, et al. Using the spleen for time-delay correction of the input function in measuring hepatic blood flow with oxygen-15 water by dynamic PET. Ann Nucl Med. 1999;13:215–21.

32. Van der Weerdt A, Klein LJ, Boellaard R, Visser CA, Visser FC, Lammertsma AA. Image-derived input functions for determination of MRGlu in cardiac ^{18}F-FDG PET scans. J Nucl Med. 2001;42:1622–9.

33. Votaw JR, Shulman SD. Performance evaluation of the pico-count flow-through detector for use in cerebral blood flow PET studies. J Nucl Med. 1998;39:509–15.

34. Watabe H, Channing MA, Riddell C, Jousse F, Libutti SK, Carrasquillo JA, et al. Noninvasive estimation of the aorta input function for measurement of tumor blood flow with. IEEE Trans Med Imaging. 2001;20:164–74.

35. Ziegler SI, Haberkorn U, Byrne H, Tong C, Kaja S, Richolt JA, et al. Price P Measurement of liver blood flow using oxygen-15 labelled water and dynamic positron emission tomography: limitations of model description. Eur J Nucl Med. 1996;23:169–77.

Comparison of Gd-DTPA-Induced Signal Enhancements in Rat Brain C6 Glioma among Different Pulse Sequences in 3-Tesla Magnetic Resonance Imaging

H. Sato, J. Enmi, N. Teramoto, T. Hayashi, A. Yamamoto, T. Tsuji, H. Naito & H. Iida

Laboratory for Diagnostic Solutions and Department of Investigative Radiology, Advanced Medical Engineering Center, Research Institute, National Cardiovascular Center, Osaka, Japan; Diagnostic Imaging Medical Affairs, Medical Affairs, Product Development Department, Bayer Yakuhin, Ltd., Osaka, Japan; Department of Radiology, Hospital of National Cardiovascular Center, Osaka, Japan

Sato H, Enmi J, Teramoto N, Hayashi T, Yamamoto A, Tsuji T, Naito H, Iida H. Comparison of gd-dtpa-induced signal enhancements in rat brain c6 glioma among different pulse sequences in 3-tesla magnetic resonance imaging. Acta Radiol 2007;000:1–8.

Background: T1-shortening contrast media are routinely used in magnetic resonance (MR) examinations for the diagnosis of brain tumors. Although some studies show a benefit of 3 Tesla (T) compared to 1.5T in delineation of brain tumors using contrast media, it is unclear which pulse sequences are optimal.
Purpose: To compare gadopentetate dimeglumine (Gd-DTPA)-induced signal enhancements in rat brain C6 glioma in the thalamus region among different pulse sequences in 3T MR imaging.
Material and Methods: Five rats with a surgically implanted C6 glioma in their thalamus were examined. T1-weighted brain images of the five rats were acquired before and after Gd-DTPA administration (0.1 mmol/kg) using three clinically available pulse sequences (spin echo [SE], fast SE [FSE], fast spoiled gradient echo [FSPGR]) at 3T. Signal enhancement in the glioma (E_T) was calculated as the signal intensity after Gd-DTPA administration scaled by that before administration. Pulse sequences were compared using the Tukey-Kramer test.
Results: E_T was 1.12 ± 0.05 for FSE, 1.26 ± 0.11 for FSPGR, and 1.20 ± 0.11 for SE. FSPGR showed significantly higher signal enhancement than FSE and comparable enhancement to SE.
Conclusion: FSPGR is superior to FSE and comparable to SE in its ability to delineate rat brain C6 glioma in the thalamus region.

Key words: Brain; contrast agents; MR imaging

Hiroshi Sato, Laboratory for Diagnostic Solutions, Advanced Medical Engineering Center, Research Institute, National Cardiovascular Center, 5-7-1 Fujishiro-dai, Suita, Osaka 565-8565, Japan (fax. +81 6 6835 5429, e-mail. camo@ri.ncvc.go.jp)

T1-shortening contrast media are routinely used in magnetic resonance (MR) examinations for the diagnosis of brain tumors. Some studies show a benefit of 3 Tesla (T) compared to 1.5T in delineation of brain tumors using contrast media (1–5). However, it is unclear which pulse sequences are optimal. The conventional spin-echo (SE) technique has been most frequently used for T1-weighted (T1W) imaging of tumors after contrast media administration. The gradient-echo (GRE) technique, which is faster than SE, was introduced initially at 1.5T or lower field strength (6–11). Some studies have reported that GRE techniques compare favorably with the SE technique for delineation of brain tumors (8–10), while other studies have reported that GRE techniques do not show contrast enhancement as well as SE (6, 7, 11). At 3T, as at 1.5T or lower field strength, the issue of whether GRE techniques are effective compared to SE has not been determined. In 16 patients, NÔBAUER-HUMANN et al. reported that 3D GRE with magnetization preparation (MPRAGE) was comparable to T1W SE in tumor-to-brain contrast at 3T, although the parameters of T1W SE were not

Acta Radiologica rad134548.3d 23/10/07 20:29:49
The Charlesworth Group, Wakefield +44(0)1924 369598 - Rev 7.51n/W (Jan 20 2003)

262880

optimized for 3T (1). In 12 patients, FISCHBACH et al. compared four T1W sequences: SE, inversion recovery fast SE (IR-FSE), 2D GRE, and MPRAGE at 3T. They observed that SE and IR-FSE provided higher contrast enhancement of brain tumors than 2D GRE and MPRAGE. Furthermore, their impressions showed that the visual quality of SE was superior to that of the other three sequences (12).

In order to compare pulse sequences, it would be preferable if the pathological and physiological conditions of subjects were constant across scans. One possible model system is the widely used rat brain glioma model (4, 5, 13–15). In most studies with small animals, MR imaging systems with small magnets are widely used. The pulse sequences available on the scanner designed for small animals, however, are different from those on a clinical scanner. By using a scanner designed for humans, we can compare diagnostic values of practical clinical pulse sequences. To our knowledge, no studies have been reported comparing pulse sequences on a 3T human scanner using a rat brain glioma model.

The purpose of the current study was to elucidate the optimal pulse sequence that provides the highest obtainable signal enhancement using gadopentetate dimeglumine (Gd-DTPA) in a rat brain C6 glioma model on a 3T human whole-body scanner.

Material and Methods

Protocols of all animal procedures were approved by the ethics committee for animal research at the National Cardiovascular Center. Male Sprague-Dawley rats (Japan SLC, Inc., Shizuoka, Japan) were used. Rats had free access to food and water, and were kept in uncrowded conditions (two/cage) in a light-, temperature-, and humidity-regulated room (light on 07.00–19.00, $23 \pm 3°C$, and $50 \pm 20\%$).

Study design

T1 measurements in the brains of three normal rats and phantom studies were performed to identify pulse sequences, among which Gd-DTPA-induced signal enhancements in rat C6 brain gliomas were compared, and to determine pulse sequence parameters. Using the determined pulse sequences and parameters, we examined five rats with developed gliomas out of 20 rats that received C6 glioma implantation in their thalamus region.

MR imaging system

All scanning was performed on a 3T whole-body scanner (Signa LX VH3M4; GE Healthcare, Milwaukee, Wisc., USA) equipped with the manufacturer's gradient system (maximum gradient strength 40 mT/m; slew rate 150 mT/m/s).

For imaging rat brains, we built a three-turn solenoid coil with a diameter of 42 mm and a length along the cylindrical axis of 18 mm. The diameter and length of this coil were adjusted to rat head size. The helical pitch of the coil was wide enough to pass the ear bars used to secure the rat's head. The coil was capable of transmission and reception, and was tuned to an impedance of $50 \, \Omega$ at a resonant frequency of 127.76 MHz. Capacitance was divided into six elements in series, which were put at each half turn. The coil was mounted on a fixing apparatus (Narishige Co., Ltd., Tokyo, Japan) using an acrylic jig specially designed for the coil (Fig. 1). Rats were placed prone on the fixing apparatus. Rat heads were secured using an incisor hook and ear bars. All components of the fixing apparatus consisted of non-magnetic materials. During imaging, the fixing apparatus, on which the rat and the coil were mounted, was placed in the gantry so that the cylindrical axis of the coil and the cranial-to-caudal direction of the rat were perpendicular to a static magnetic field, and the center of the rat brain was positioned at the magnet isocenter.

Measurement of T1 in normal rat brain

This measurement was performed to establish the normal T1 value in the transplantation site (thalamus) of the C6 glioma cells. T1 values in the brain of three normal rats (9–13 weeks old, 380 ± 50 g) were
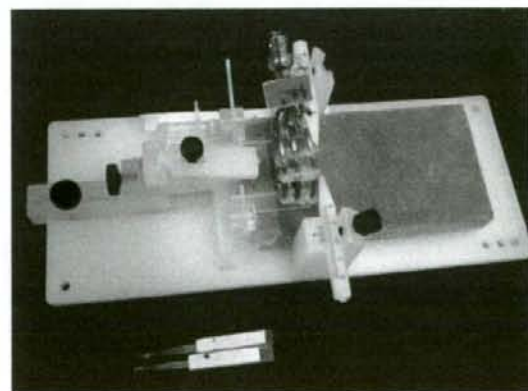

Fig. 1. The three-turn solenoid coil and the fixing apparatus used for the imaging of rats in the present study. The coil was mounted on the fixing apparatus using the specially designed acrylic jig.

262880

measured by using a saturation recovery method with a variable repetition time (TR) SE imaging sequence (16): TR 600, 1000, 2000, 4000, 8000 ms; echo time (TE) 10 ms; bandwidth (BW) 16 kHz; field of view (FOV) 40×30 mm; matrix size 256×160; slice thickness 1 mm; slice gap 1 mm; number of slices 16; number of excitations (NEX) 1; coronal plane. An 8-cm polyvinyl chloride tube with an outer diameter of 2.7 mm was inserted into the animal's trachea, and the rats were ventilated with an average of 2–3 ml per breath of a mixture of O_2, N_2, and air (2:1:10) using a small animal ventilator (CWE SAR-830/AP Ventilator; CWE, Inc., Ardmore, Pa., USA) at an average of 80 breaths per minute. Body temperature was monitored rectally ($36.0 \pm 0.5°C$).

T1 values were estimated on a pixel-by-pixel basis using the non-linear least-square fit of the signal intensity measured for each TR value. In the obtained T1 images, regions of interest (ROIs) were placed on the thalamus, hippocampus, olfactory bulb, cerebral cortex, corpus callosum, midbrain, cerebellum, pons, cerebrospinal fluid, and muscle. Mean T1 values were calculated from each ROI. A mean and a standard deviation of the mean values obtained from three rats were calculated.

Phantom study

Phantom preparation. Gd-DTPA (Magnevist; Bayer Schering Pharma, Osaka, Japan) was diluted with saline to obtain 19 solutions with different concentrations (0, 0.01, 0.03, 0.05, 0.07, 0.1, 0.15, 0.2, 0.25, 0.3, 0.5, 0.7, 1, 3, 5, 7, 10, 30, and 50 mM). Each solution was encapsulated in separate polypropylene vials with a diameter of 27 mm, which were set in agar.

T1 measurement. T1 values of each Gd-DTPA solution were measured at room temperature using the same pulse sequence as the T1 measurement in normal rats: TR 34, 100, 200, 400, 600, 800, 1000, 1200, 1400, 1600, 1800, 2000, 4000, 6000, 8000, 11,000, 15,000 ms; TE 9 ms; BW 16 kHz; FOV 210×158 mm; matrix size 256×192; slice thickness 3 mm; number of slices 1; NEX 1. A standard quadrature birdcage head coil was used.

Circular ROIs with 70–80% of the diameter of a vial were placed on a homogeneous signal portion of each phantom image. T1 values were estimated by non-linear least-square fit of the average signal intensity of all voxels in the ROI measured for each TR value. Five measurements were performed for phantoms, and the mean and standard deviation of measured T1 values were calculated.

Choice of pulse sequences. We used a Gd-DTPA saline solution (0.1 mM) with a T1 value close to that in the normal thalamus as a corresponding solution to the glioma in the thalamus region before contrast. We hypothesized that T1 in the glioma would not be so different from that in normal tissue. Saline solutions with a higher concentration of Gd-DTPA were regarded as a corresponding solution to the glioma after contrast.

T1W images of each phantom were acquired at room temperature (approximately 21°C) using four clinically available pulse sequences (SE, fast SE [FSE], IR-FSE [T1FLAIR], and fast spoiled GRE [FSPGR]) (Table 1). A standard quadrature birdcage head coil was used for the imaging of phantoms.

Circular ROIs with 70–80% of the diameter of the vial were placed on a uniform signal portion of each phantom. Mean signal intensities were calculated from each ROI. For each sequence, signal enhancements of each Gd-DTPA solution (E_P) were calculated as $E_P = S/S_0$, where S is the signal intensity of each solution and S_0 is that of 0.1 mM of the solution. The pulse sequences showing high E_P were used for the imaging of C6 glioma model rats and were compared based on Gd-DTPA-induced signal enhancements in brain tumors, delineated by histopathology.

Rat brain C6 glioma model study
Preparation of rat brain C6 glioma models. C6 glioma cells (CCL-107 cell line, ATCC; Summit Pharmaceuticals International Corporation, Tokyo,

Table 1. Pulse sequences and imaging parameters used for imaging of saline phantoms containing gadopentetate dimeglumine (Gd-DTPA)

Pulse sequence	TR, ms	TE, ms	TI, ms	FA, °	ETL	BW, kHz	NEX	Acquisition time, min:s
SE	1400	14	—	—	—	16	1	4:46
FSE	1400	16	—	—	3	32	1	1:52
T1FLAIR	3000	16	1300	—	3	32	1	4:00
FSPGR	20	3.2	—	30	—	32	10	0:39

For all pulse sequences, FOV was 210×158 mm, matrix was 256×192, the number of slices was 1, and the slice thickness was 3 mm. SE: spin echo; FSE: fast spin echo; T1FLAIR: inversion recovery fast spin echo; FSPGR: fast spoiled gradient echo; TR: repetition time; TE: echo time; TI: inversion time; FA: flip angle; ETL: echo train length; BW: bandwidth; NEX: number of excitations.

262880

Japan) were implanted into the region of the thalamus in the left hemispheres of the brains of 20 rats (8 weeks old, 292.8 ± 14.8 g). The implantation procedures were performed under general anesthesia using an intramuscular injection of ketamine (33 mg/kg; Sankyo Co., Ltd., Tokyo, Japan) and xylazine (7 mg/kg; Bayer AG, Leverkusen, Germany). A burr hole was made 3 mm lateral and 2 mm posterior to the bregma using a dental drill. A needle with an outer diameter of 0.3 mm was inserted 4 mm below the outer table of the skull through the burr hole. A 10-μl solution containing 10^7 cells/ml was infused over 5 min at a constant rate using a microsyringe (Hamilton Co., Reno, Nev., USA) and infusion pump (Eicom Corp., Kyoto, Japan).

MR imaging. Two weeks after implantation, all 20 rats underwent screening by T1W imaging after Gd-DTPA administration. Developed glioma was confirmed in only five out of 20 rats. Those five rats were used for experiments for the comparison of pulse sequences. Three weeks after implantation, when the glioma was fully developed, T1W brain images of the selected five rats (11 weeks old, 301.3 ± 29.0 g) were acquired before and after Gd-DTPA administration using three pulse sequences determined by the phantom study (Table 2) in the coronal plane. Rats were given general anesthesia with an intramuscular injection of a ketamine (33 mg/kg) and xylazine (7 mg/kg) mixture, and allowed to breathe spontaneously during preparation and imaging. First, precontrast T1W images were acquired. Then, a dose of 0.1 mmol/kg of Gd-DTPA was administered by hand injection followed by a 3.0-ml saline flush through a 22G indwelling needle placed in a tail or femoral vein. Postcontrast T1W imaging started 1 min after Gd-DTPA administration with identical settings to the precontrast imaging. Each rat was examined using all three pulse sequences (Table 2). In order to eliminate the effect of previously administered Gd-DTPA, three scans using different pulse sequences

were performed on three separate days, at 22- to 26-hour intervals, in a randomized order.

ROI analysis. Based on the results of histopathology (see below), ROIs were placed on a portion of each glioma. Areas of necrosis or hemorrhage were excluded from the ROI. Mean signal intensities in the pre- and postcontrast T1W images were calculated from each ROI. For each sequence, signal enhancement of each glioma (E_T) was calculated as $E_T = S_{post}/S_{pre}$, where S_{post} is signal intensity in the glioma after contrast and S_{pre} is that before contrast.

Histopathology
One day after MR imaging, rat brains were removed and fixed in formalin. All brains were completely coronally sectioned. Sections were stained with hematoxylin and eosin (HE) in order to delineate areas of glioma, hemorrhage, and necrosis.

Statistical analysis
All parameters assessed were given as means ± standard deviations. Pair-wise comparison among pulse sequences was performed using the Tukey-Kramer test. A P value of <0.05 was considered statistically significant.

Results

T1 in normal rat brains
Fig. 2 shows images from one of the three normal rats used to quantitate T1 values in the brain. Table 3 summarizes the T1 values of typical brain structures. The T1 value in the thalamus was 1405 ± 32 ms.

T1 of Gd-DTPA solutions
Fig. 3 shows selected images from a series of 17 images obtained with different TR values. Table 4 summarizes T1 values in the Gd-DTPA solutions

Table 2. Pulse sequences and imaging parameters used for imaging of rat brains with C6 glioma cell implants

Pulse sequence	TR, ms	TE, ms	FA, °	ETL	BW, kHz	NEX	Acquisition time, min:s
SE	1400	13	—	—	16	1	4:46
FSE	1400	18.6	—	3	32	3	4:32
FSPGR	20	4.7	30	—	32	8	5:40

For all pulse sequences, FOV was 60×45 mm, matrix was 256×192, the number of slices was 11, and the slice thickness was 2.5 mm (0.5-mm gap). SE: spin echo; FSE: fast spin echo; FSPGR: fast spoiled gradient echo; TR: repetition time; TE: echo time; FA: flip angle; ETL: echo train length; BW: bandwidth; NEX: number of excitations.
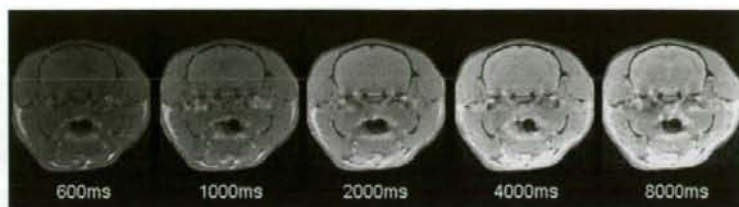
262880

Fig. 2. Images from one of three rats used for the measurement of T1 values in normal rat brain. One of 16 slices acquired is shown. The images are arranged from left to right in ascending order of repetition time. All five images are set with equal window width and equal window level.

Table 3. T1 relaxation time in normal rat brain at 3T

	T1, ms
Thalamus	1405 ± 32
Hippocampus	1779 ± 151
Olfactory bulb	1613 ± 117
Cerebral cortex	1506 ± 13
Corpus callosum	1389 ± 43
Midbrain	1329 ± 50
Cerebellum	1726 ± 356
Pons	1343 ± 80
Cerebrospinal fluid	3460 ± 737
Muscle	1529 ± 99

Mean and standard deviation of values obtained from three rats.

Table 4. T1 of saline with different concentrations of Gd-DTPA at 3T

Gd-DTPA concentration, mM	T1, ms
0	3026 ± 121
0.01	2652 ± 96
0.03	2245 ± 108
0.05	1970 ± 92
0.07	1775 ± 103
0.1	1302 ± 54
0.15	993 ± 57
0.2	820 ± 52
0.25	737 ± 51
0.3	666 ± 63
0.5	389 ± 17
0.7	284 ± 12
1	209 ± 9
3	84 ± 4
5	58 ± 2
7	36 ± 1
10	27 ± 1
30	—
50	—

Mean and standard deviation of values obtained from five measurements.

ranging from 0 to 10 mM. In 30 and 50 mM solutions, an accurate T1 value could not be measured because of extensive signal loss due to T2 decay. The 0.1-mM solution showed a T1 value (1302 ± 54 ms) closest to that in the normal thalamus (1405 ± 32 ms).
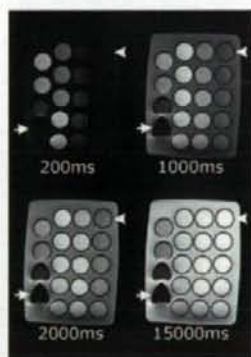

Fig. 3. Images obtained in the measurement of T1 values of 19 saline solutions with different concentrations of gadopentetate dimeglumine (0, 0.01, 0.03, 0.05, 0.07, 0.1, 0.15, 0.2, 0.25, 0.3, 0.5, 0.7, 1, 3, 5, 7, 10, 30, and 50 mM). The four selected images from a series of 17 images obtained with different TR values are shown. Each solution was encapsulated in separate polypropylene vials, which were set in agar. The concentration of gadopentetate dimeglumine decreases from bottom to top and from left to right. Arrows and arrowheads denote the 50-mM and 0-mM solutions, respectively. All four images are set with equal window width and equal window level.

Choice of pulse sequences

Fig. 4 shows E_P in the Gd-DTPA solutions ranging from 0.1 to 50 mM. In Gd-DTPA solutions ranging from 0.15 to 30 mM, a higher E_P was obtained as follows: FSPGR > SE > FSE > T1FLAIR. Because E_P for T1FLAIR was lowest at all concentrations, T1FLAIR was not used for the imaging of rat brain tumors.

Based on our preliminary experiments, the T1 value in the glioma in the thalamus region after contrast was about 90% of that before contrast. Therefore, we regarded the 0.15-mM solution as a corresponding solution to glioma after contrast, and compared E_P values at 0.15 mM obtained using different sequences (Fig. 5). E_P at 0.15 mM was 1.10 ± 0.02 for FSE, 1.16 ± 0.01 for FSPGR, 1.16 ± 0.01 for SE, and 1.06 ± 0.01 for T1FLAIR. The Tukey-Kramer test showed significant differences ($P < 0.05$) between all pairs except for FSPGR–SE. E_P for FSPGR was significantly higher than that for FSE and T1FLAIR and comparable to that for SE.
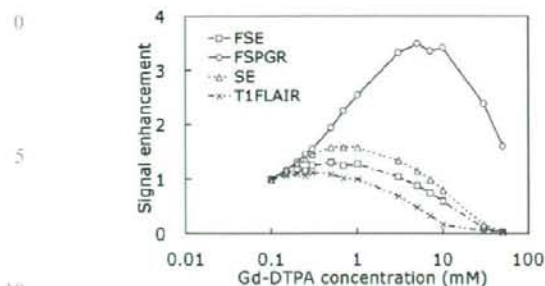
262880

Fig. 4. Signal enhancements in saline solutions containing gadopentetate dimeglumine (Gd-DTPA) obtained by the following pulse sequences: spin echo (SE); fast spin echo (FSE); inversion recovery fast spin echo (T1FLAIR); fast spoiled gradient echo (FSPGR). Signal enhancement was the signal intensity scaled by that of a 0.1-mM Gd-DTPA solution whose T1 value was closest to the average T1 value in the brain parenchyma of normal rats.

Signal enhancement in rat brain C6 glioma

Fig. 6 displays typical pre- and postcontrast T1W images of brains of C6 glioma model rats, together with an example of ROIs placed on the glioma and HE-stained slices. Fig. 7 shows the comparison between E_T values for FSE, SE, and FSPGR. E_T values were 1.12 ± 0.05 for FSE, 1.26 ± 0.11 for FSPGR, and 1.20 ± 0.11 for SE. The Tukey-Kramer test showed the significant superiority of FSPGR over FSE. There was no significant difference between FSPGR and SE.

Discussion

T1W imaging using SE results in a corresponding restriction in the number of slices as a result of the
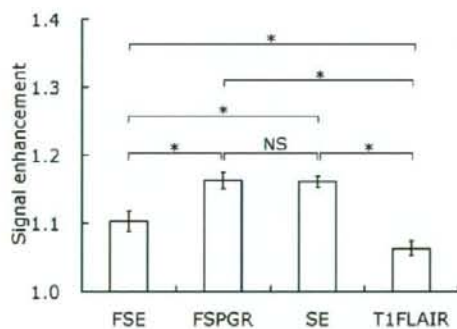

Fig. 5. Signal enhancement of saline solution with 0.15 mM Gd-DTPA obtained using different pulse sequences: spin echo (SE); fast spin echo (FSE); inversion recovery fast spin echo (T1FLAIR); fast spoiled gradient echo (FSPGR). Signal enhancement was defined as the signal intensity of a 0.15-mM solution scaled by that of a 0.1-mM solution. The Tukey-Kramer test was performed for pair-wise comparison among four pulse sequences. The asterisk and NS denote significant difference ($P < 0.05$) and no significant difference ($P > 0.05$), respectively.
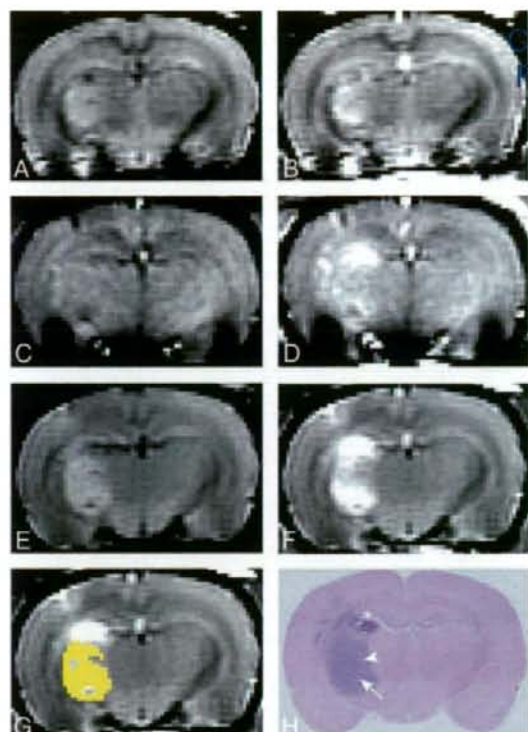
Fig. 6. Examples of pre- (A, C, E) and post-contrast (B, D, F) coronal T1-weighted images obtained using fast spin-echo (FSE) (A, B), fast spoiled gradient-echo (FSPGR) (C, D), and spin-echo (SE) (E, F) sequences. A region of interest (ROI) placed on the glioma (G) and a slice stained using hematoxylin and eosin (HE) (H). T1-weighted images were acquired 3 weeks after the implantation of C6 glioma cells. Areas of necrosis or hemorrhage, which were delineated based on histopathology, were excluded from ROIs. In the HE-stained slice, small-cell glioma (arrowhead), hemorrhage (asterisk), and necrosis (arrow) were found.
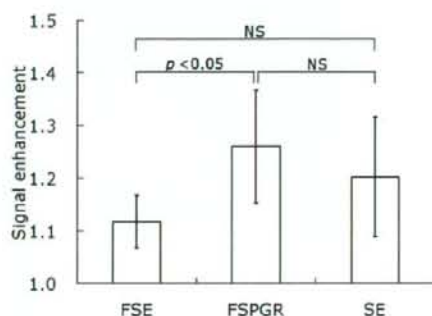
Fig. 7. Signal enhancement in rat brain C6 glioma obtained with different pulse sequences: spin echo (SE); fast spin echo (FSE); fast spoiled gradient echo (FSPGR). Signal enhancement was defined as the signal intensity after Gd-DTPA administration scaled by that before administration. The pair-wise comparison among pulse sequences was performed using the Tukey-Kramer test. NS denotes no significant difference ($P > 0.05$).

Acta Radiol 2007 (000)

156

Acta Radiologica rad134548.3d 23/10/07 20:33:27
The Charlesworth Group, Wakefield +44(0)1924 369598 - Rev 7.51n/W (Jan 20 2003)

262880

specific absorption rate (SAR) at 3T. The use of FSE makes radiofrequency heating more serious. Compared to SE and FSE, FSPGR provides relatively low radiofrequency heating and, if the NEX of FSPGR can be reduced, relatively short acquisition time. This depends on the signal-to-noise ratio, and we thought it possible based on our rat brain images (Fig. 6). Therefore, we examined the characteristics of signal enhancement in FSPGR. FSPGR provided significantly higher signal enhancement than FSE and comparable signal enhancement to SE, both in the 0.15-mM Gd-DTPA solution and in rat brain C6 glioma in the thalamus region. We speculate that FSPGR may be superior to FSE and comparable to SE in its ability to delineate brain tumors, although, in order to verify this speculation, several studies would be required using different cell types and various transplantation sites. Considering the advantage of FSPGR in terms of acquisition time and SAR limit, FSPGR may be more suitable for contrast-enhanced T1W imaging of brain tumors in clinical 3T scanners than SE. Additionally, high-resolution 3D images can be obtained by using FSPGR with a reasonable acquisition time so that small lesions may be better visualized. On the other hand, FSPGR was more sensitive to magnetic susceptibility artifacts than SE (Fig. 6). SE could therefore be more suitable than FSPGR for delineation of tumors in regions with susceptibility artifacts, such as the base of the skull.

E_T values obtained in our study (1.26 for FSPGR, 1.20 for SE, and 1.12 for FSE) were lower compared to previously reported values (1, 4, 5, 12). For example, RUNGE et al. reported that the E_T induced by Gd-DTPA was approximately 1.44 using SE in rat brain C6/LacZ glioma models at 3T (5). The difference between E_T in our study and that in previous reports may result from the difference in the type of tumor, in the degree of growth of brain tumors, or in TR. In our study, TR was adjusted to increase T1 contrast in the normal brain region for specification of more exact location of the glioma. Although the use of a shorter TR may increase signal enhancement in the glioma, contrast in the normal region would become unclear, and therefore it could become difficult to specify the location of the glioma exactly. Therefore, we used a longer TR than that in previous reports.

FISCHBACH et al. showed higher contrast in SE in patients, but they optimized the TR (600 ms) of SE by phantom experiments using a saline solution with a low concentration of Gd-DTPA (0.125 μM) (12), whose T1 is extremely long compared to that in the brain. We quantified T1 in rat brains and chose a proper TR (1400 ms) of SE to enhance normal brain contrast. Therefore, our comparison would be fairer and our results may be more closely extrapolated to human tumors.

One limitation of our work is our limited sample size. Although C6 glioma cells were implanted into 20 rats in our in-vivo study, only five rats could be used for the experiment, as C6 gliomas showed considerable individual variation in their growth and were fully developed only in five rats. Therefore, the number of test animals was relatively small, resulting in large standard deviations for E_T. A larger sample size may show a significant difference between FSPGR and SE.

In conclusion, FSPGR is superior to FSE and comparable to SE in its ability to delineate rat brain C6 glioma in the thalamus region using venous injection of Gd-DTPA.

References

1. Nöbauer-Huhmann IM, Ba-Ssalamah A, Mlynarik V, Barth M, Schoggl A, Heimberger K, et al. Magnetic resonance imaging contrast enhancement of brain tumors at 3 tesla versus 1.5 tesla. Invest Radiol 2002;37:114–9.
2. Trattnig S, Ba-Ssalamah A, Noebauer-Huhmann IM, Barth M, Wolfsberger S, Pinker K, et al. MR contrast agent at high-field MRI (3 Tesla). Top Magn Reson Imaging 2003;14:365–75.
3. Ba-Ssalamah A, Nöbauer-Huhmann IM, Pinker K, Schibany N, Prokesch R, Mehrain S, et al. Effect of contrast dose and field strength in the magnetic resonance detection of brain metastases. Invest Radiol 2003;38:415–22.
4. Biswas J, Nelson CB, Runge VM, Wintersperger BJ, Baumann SS, Jackson CB, et al. Brain tumor enhancement in magnetic resonance imaging: comparison of signal-to-noise ratio (SNR) and contrast-to-noise ratio (CNR) at 1.5 versus 3 tesla. Invest Radiol 2005;40: 792–7.
5. Runge VM, Biswas J, Wintersperger BJ, Baumann SS, Jackson CB, Herborn CU, et al. The efficacy of gadobenate dimeglumine (Gd-BOPTA) at 3 Tesla in brain magnetic resonance imaging: comparison to 1.5

Tesla and a standard gadolinium chelate using a rat brain tumor model. Invest Radiol 2006;41:244–8.

6. Chappell PM, Pelc NJ, Foo TK, Glover GH, Haros SP, Enzmann DR. Comparison of lesion enhancement on spin-echo and gradient-echo images. Am J Neuroradiol 1994;15:37–44.

7. Rand S, Maravilla KR, Schmiedl U. Lesion enhancement in radio-frequency spoiled gradient-echo imaging: theory, experimental evaluation, and clinical implications. Am J Neuroradiol 1994;15:27–35.

8. Pui MH, Fok EC. MR imaging of the brain: comparison of gradient-echo and spin-echo pulse sequences. Am J Roentgenol 1995;165:959–62.

9. Fellner F, Holl K, Held P, Fellner C, Schmitt R, Bohm-Jurkovic H. A T1-weighted rapid three-dimensional gradient-echo technique (MP-RAGE) in preoperative MRI of intracranial tumours. Neuroradiology 1996;38: 199–206.

10. Li D, Haacke EM, Tarr RW, Venkatesan R, Lin W, Wielopolski P. Magnetic resonance imaging of the brain with gadopentetate dimeglumine-DTPA: comparison of T1-weighted spin-echo and 3D gradient-echo sequences. J Magn Reson Imaging 1996;6:415–24.

11. Elster AD. How much contrast is enough? Dependence of enhancement on field strength and MR pulse sequence. Eur Radiol 1997;7 Suppl 5:276–80.

12. Fischbach F, Bruhn H, Pech M, Neumann F, Ricke J, Felix R, et al. Efficacy of contrast medium use for neuroimaging at 3.0 T: utility of IR-FSE compared to other T1-weighted pulse sequences. J Comput Assist Tomogr 2005;29:499–505.

13. Raila FA, Bowles AP Jr, Perkins E, Terrell A. Sequential imaging and volumetric analysis of an intracerebral C6 glioma by means of a clinical MRI system. J Neurooncol 1999;43:11–7.

14. Thorsen F, Ersland L, Nordli H, Enger PO, Huszthy PC, Lundervold A, et al. Imaging of experimental rat gliomas using a clinical MR scanner. J Neurooncol 2003;63:225–31.

15. Blanchard J, Mathieu D, Patenaude Y, Fortin D. MR-pathological comparison in F98-Fischer glioma model using a human gantry. Can J Neurol Sci 2006;33: 86–91.

16. Wansapura JP, Holland SK, Dunn RS, Ball WS Jr. NMR relaxation times in the human brain at 3.0 tesla. J Magn Reson Imaging 1999;9:531–8.

262880

NOTE

Acceleration of Monte Carlo-based scatter compensation for cardiac SPECT

A Sohlberg[1,2], H Watabe[1] and H Iida[1]

[1] National Cardiovascular Center Research Institute, 5-7-1 Fujishiro-dai, Suita City, 565-8565 Osaka, Japan
[2] HERMES Medical Solutions, Skeppsbron 44, 111 30 Stockholm, Sweden

E-mail: antti.sohlberg@hermesmedical.com

Abstract

Single proton emission computed tomography (SPECT) images are degraded by photon scatter making scatter compensation essential for accurate reconstruction. Reconstruction-based scatter compensation with Monte Carlo (MC) modelling of scatter shows promise for accurate scatter correction, but it is normally hampered by long computation times. The aim of this work was to accelerate the MC-based scatter compensation using coarse grid and intermittent scatter modelling. The acceleration methods were compared to un-accelerated implementation using MC-simulated projection data of the mathematical cardiac torso (MCAT) phantom modelling ^{99m}Tc uptake and clinical myocardial perfusion studies. The results showed that when combined the acceleration methods reduced the reconstruction time for 10 ordered subset expectation maximization (OS-EM) iterations from 56 to 11 min without a significant reduction in image quality indicating that the coarse grid and intermittent scatter modelling are suitable for MC-based scatter compensation in cardiac SPECT.

1. Introduction

The quality of single proton emission computed tomography (SPECT) is degraded by attenuation, collimator blurring and scatter. Whereas attenuation and collimator blurring can nowadays be corrected in clinically acceptable times, accurate and efficient scatter correction has been proven to be a more difficult problem. This is mainly due to the fact that the shape of the scatter point-spread function depends on the location inside the object and can be very difficult to parametrize.

One very promising recently presented scatter compensation method is the Monte Carlo (MC)-based scatter correction by Beekman *et al* (2002). In this method, a MC simulator is used as a forward-projector for scatter in the ordered subset expectation maximization

(OS-EM) algorithm (Hudson and Larkin 1994). MC-based scatter modelling is expected to be especially advantageous in areas where the attenuating media is highly non-uniform such as the thorax, because it can faithfully produce the complex shape of the scatter response function. The MC-based scatter compensation has been shown to outperform the common triple-energy window scatter compensation method in terms of contrast and myocardial lesion detectability (Xiao *et al* 2006). Unfortunately, despite the considerable advances made in MC-based scatter compensation its widespread utilization in clinical practice can still be limited by long computation times.

Kadrmas *et al* (1998) have presented two simple and effective acceleration methods for reconstruction-based scatter compensation. The first of these approaches is the coarse grid scatter modelling method, which calculates the scatter contribution using sparser grid than is used in the actual reconstruction. The second approach is the intermittent scatter modelling method, where scatter is modelled only during the first couple of OS-EM iterations and then held as a constant additive factor for the later iterations. Both of these approaches are based on the assumption that the scatter response contains mainly low-frequency components and can thus be modelled with a relatively large voxel size and not during the last OS-EM iterations. Kadrmas *et al* presented their acceleration methods for the effective scatter source estimation method (Frey and Tsui 1996) and showed that the performance of the accelerated scatter compensation was very similar to the performance of the standard (un-accelerated) scatter correction.

The goal of this work was to implement the coarse grid and intermittent scatter modelling methods for MC-based scatter compensation and to evaluate their performance in case of ^{99m}Tc cardiac SPECT.

2. Materials and methods

2.1. Implementation of the MC simulator

MC simulations are based on sampling radioactive decays within a source volume and following their interactions inside the attenuating media. Our MC simulator uses four different maps in the simulations: emission map for setting photons to be tracked, density map for sampling interactions and primary and scatter maps for storing photon weights. The history of each photon (primary or scatter) in our simple MC simulator is tracked shortly as follows:

(1) If the simulated photon is a primary the primary map is updated. Otherwise direction cosines are sampled and random walk is started for the scatter photon.

(2) Photon interaction points are calculated using the delta scattering algorithm (Woodcock *et al* 1965), which does not require ray tracing through the attenuating media. The basic principle of delta scattering is that the path-length P between two 'fictious' interaction points is sampled as $P = -\ln(R)/\mu_{max}$, where R is a uniform random number and μ_{max} is the largest attenuation coefficient in the attenuating media (Ljungberg *et al* 2005). At the end of the sampled path a possible interaction is sampled according to established methods or tracking is continued by sampling a new distance P according to the above-mentioned equation.

(3) At each real interaction point photon weight is multiplied by the probability that no photoelectric effect occurred and a copy of the original photon is forced to Compton scatter towards the detector and scatter map is updated according to the convolution-based forced detection approach (de Jong *et al* 2001).

(4) If predetermined number of scattering events has not been reached, the history of the original photon is continued by Compton scatter. New direction cosines are sampled from the Klein–Nishina function and tracking is continued from (2).

After all the photons have been simulated the primary and scatter maps are multiplied by probability that photon emitted from a certain voxel reaches the detector without interaction. Then these maps are convolved with depth-dependent detector response function, which is assumed to be Gaussian. The blurred primary and scatter maps are finally forward-projected to primary and scatter projections.

2.2. Implementation of the reconstruction algorithm with MC-based scatter compensation

The developed MC simulator was included into an OS-EM reconstruction algorithm as forward-projector for the scattered counts as originally proposed by Beekman et al (2002). The OS-EM is given by

$$f_j^{\text{new}} = \frac{f_j^{\text{old}}}{\sum_{i \in S_n} a_{ij}} \sum_{i \in S_n} a_{ij} \frac{p_i}{\sum_k a_{ik} f_k^{\text{old}} + s_i}, \tag{1}$$

where f is the reconstructed image, p is the measured projections, j (or k) is the reconstruction voxel index, i is the projection pixel index, a_{ij} is the probability that emission from voxel j is detected in pixel i, s is the MC-based scatter projections and S_n is the nth subset. The image update in OS-EM consists of sequential forward- and back-projection operations. The estimated projections are obtained by forward-projecting the current image estimate $\left(\sum_k a_{ik} f_k^{\text{old}}\right)$, and correction terms that are used to update the old image are formed by back-projecting the ratio of the measured and estimated + scatter projections $\left(\sum_{i \in S_n} a_{ij} \frac{p_i}{\sum_k a_{ik} f_k^{\text{old}} + s_i}\right)$.

In this work the forward- and back-projectors were implemented as rotation based (Di Bella et al 1996). The back-projector included attenuation and detector response compensation and the forward-projector attenuation, detector response and MC-based scatter compensation. Attenuation correction factors for each voxel were calculated simply by summing the rotated attenuation map along columns. Detector response, on the other hand, was modelled by convolving each plane of the reconstruction matrix parallel to the projection plane with collimator response kernel, which was assumed to be Gaussian. The scatter projection for each projection angle was obtained by MC-based forward-projection of the current image estimate.

2.3. Acceleration of MC-based scatter compensation

The coarse grid scatter modelling method was implemented by simply down-sampling the current image estimate (and the attenuation map) into a sparser matrix before the MC-based forward-projection and linearly interpolating the scatter projections back to the original size after forward-projection was finished. In the intermittent acceleration approach the MC-based scatter modelling is performed only in the few early OS-EM iterations and after that the scatter projections are kept fixed for remaining iterations.

2.4. Performance tests

Performance tests were performed using a female version of the mathematical cardiac torso (MCAT) phantom (Tsui et al 1994), and the camera parameters are shown in table 1. The MCAT phantom modelled normal human tissue densities in the thorax region and the source distribution presented the ^{99m}Tc uptake with the following relative activities per
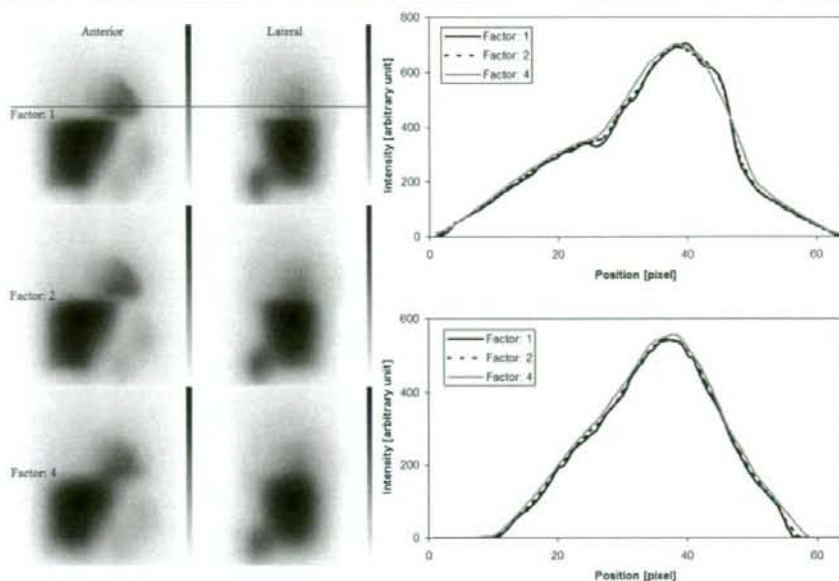
Figure 1. Comparison of scatter projections and profiles obtained with different down-sampling factors (factor: 1 is scatter projection without down-sampling). Upper profile is obtained from the anterior projection and lower from the lateral projection. Locations of the profiles are shown as horizontal lines.

Table 1. Camera parameters for Monte Carlo simulations.

Low-energy high-resolution collimator (4.0 cm hole length, 0.178 cm hole diameter)
0.4 cm intrinsic detector resolution
9.0% energy resolution
15.0% energy window centred on 140 keV
23.0 cm radius of rotation

voxel: myocardium 100, liver 50, kidney 100, spleen 80, lung 5 and rest of the body 2.5. Two lesions (anterior and inferior) with the relative uptake of 2.5 were included in the left myocardium.

The effects of different down-sampling factors in the coarse grid scatter modelling scheme were studied by performing MC simulations using the MCAT phantom. The pixel size was set to 0.625 cm (64×64 projection and $64 \times 64 \times 64$ image matrix size). Down-sampling factors of 2 ($64 \times 64 \times 64$ image matrix down-sampled to $32 \times 32 \times 32$ matrix) and 4 ($64 \times 64 \times 64$ image matrix down-sampled to $16 \times 16 \times 16$ matrix size) were investigated. Figure 1 presents anterior and lateral scatter projection images of the MCAT phantom. According to this figure factor 4 produces slightly distorted scatter projections, and thus the down-sampling factor was set to 2 for all the reconstructions accelerated with the coarse grid scatter modelling.

The effect of the number of scatter update iterations was studied by using MCAT projection data simulated using the SIMIND MC simulator (Ljungberg and Strand 1989). The camera parameters for this simulation are again shown in table 1. The number of simulated noise-free
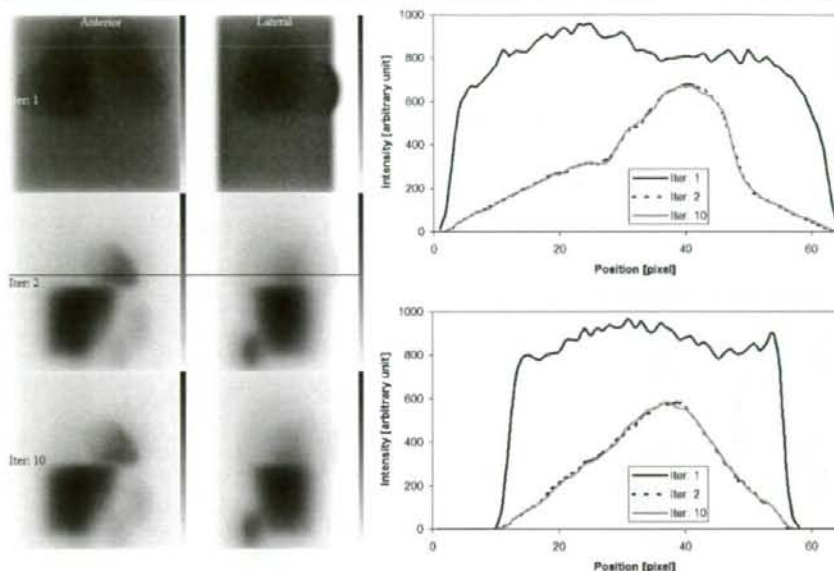
Figure 2. Comparison of different number of scatter update iterations. Upper profile is obtained from the anterior projection and lower from the lateral projection. Locations of the profiles are shown as horizontal lines.

projections was 64 on a 360° orbit and pixel size was 0.3125 cm (128×128 projection and $128 \times 128 \times 128$ image matrix size). The projections were collapsed to a 64×64 matrix size before the reconstruction. Reconstruction using the noise-free projection data was performed with 16 subsets and 1–10 iterations, and the MC forward-projected scatter projections were saved after every iteration. Figure 2 presents scatter projection images and profiles for different iteration numbers, and these images show that the scatter projections do not change markedly after two iterations. Therefore, in the following performance tests only two scatter iterations were used when intermittent scatter modelling was applied.

The acceleration methods were tested using the same MCAT projection data that were used to find the scatter iterations stopping point. Poisson noise was added to the noise-free projections by setting number of total counts to 5 million. The projections were reconstructed without scatter compensation, with the MC-based scatter compensation but without acceleration, with coarse grid scatter modelling (down-sampling factor of 2), with intermittent scatter modelling (scatter updated during the first two iterations) and with both accelerations applied at the same time. Number of MC simulated photons per projection angle was set to 1.0 million and 16 subsets with 10 iterations were used. After reconstruction images were filtered with a 3D Butterworth filter (order: 5, cutoff: 1.0 cm^{-1}), transverse slices were zoomed and reoriented into short-axis slices. Regions of interest (ROI) were drawn on the normal myocardium, ventricle and on the anterior/inferior defect areas. Normal myocardium to ventricle and normal myocardium to lesion contrasts were calculated.

In addition to Monte Carlo simulations the acceleration methods were also tested using a clinical ^{99m}Tc myocardial stress/rest perfusion study acquired with the Siemens Symbia SPECT/CT scanner. Low-energy high-resolution parallel hole collimators were used, and
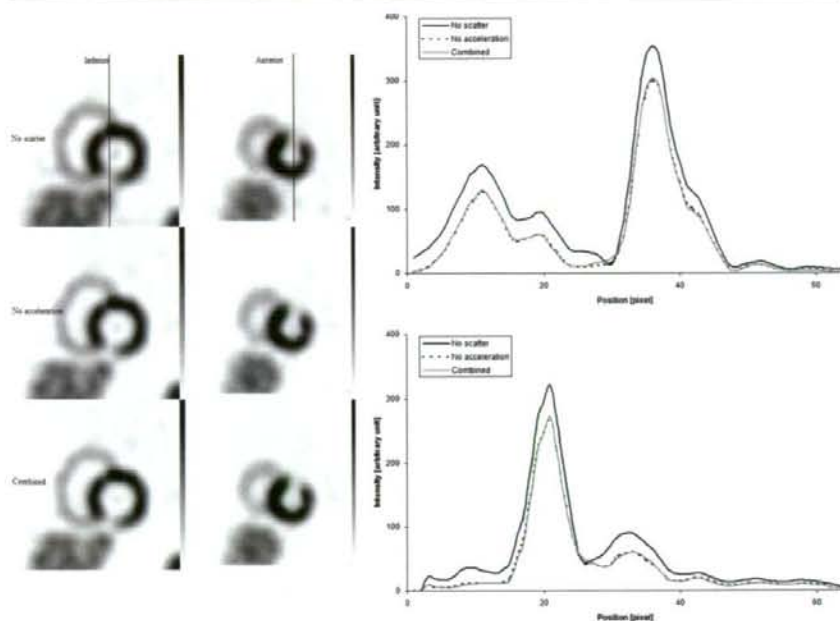
Figure 3. Short-axis slices and profiles through the heart of the MCAT phantom for reconstruction without scatter compensation (no scatter) and with MC-based scatter compensation without acceleration (no acceleration) and with coarse grid + intermittent scatter modelling (combined). Results for other acceleration methods are not shown, because they overlap the coarse grid + intermittent scatter compensation profiles. Upper profile is obtained from the image with inferior lesion and lower with anterior lesion. Locations of the profiles are shown as vertical lines.

Table 2. Lesion-to-normal myocardium and ventricle-to-normal myocardium contrasts for different MC-based scatter compensation acceleration schemes.

Scatter compensation method	Acceleration method	Contrast		
		Anterior	Inferior	Ventricle
No compensation		0.57	0.51	0.80
MC-based	No acceleration	0.64	0.58	0.91
	Coarse grid	0.65	0.59	0.93
	Intermittent	0.62	0.60	0.93
	Coarse grid+intermittent	0.64	0.59	0.93

60 projection angles over a 180° arc were acquired using a symmetric 15% energy window centred at 140 keV.

3. Results

Figure 3 shows short-axis slices and profiles through the left ventricle of the MCAT phantom for reconstruction without scatter compensation and with the MC-based scatter compensation without acceleration and with coarse grid + intermittent scatter modelling. Profiles for the
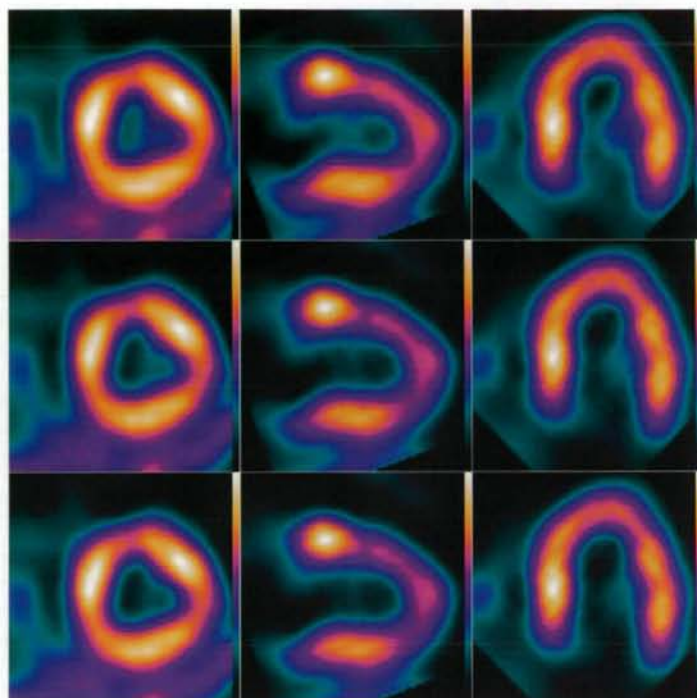
Figure 4. Example short-axis (first column), vertical long-axis (second column) and horizontal long-axis (third column) slices from a clinical rest myocardial perfusion study for reconstruction without scatter compensation (first row), with MC-based scatter compensation without acceleration (second row) and with coarse grid +intermittent scatter modelling (third row).

un-accelerated and accelerated scatter compensation practically overlap indicating similar performance. This same conclusion can also be drawn from table 2, which presents the lesion and ventricle contrasts. All the scatter compensation methods offer very similar contrast values and clearly improve contrast when compared to reconstruction without scatter compensation.

Figure 4 presents results for the resting clinical study (for the stress study the findings in image quality were identical to the resting study). It can be seen that the images reconstructed with and without MC-based scatter compensation acceleration are nearly identical. Table 3 presents the approximate reconstruction times for different scatter compensation methods.

4. Discussion

The aim of this study was to accelerate the MC-based scatter compensation using the coarse grid and intermittent scatter modelling methods. Both of these acceleration methods proved to provide clear improvement in execution times without any marked degradation in image quality when compared to un-accelerated version of MC-based scatter-compensation (tables 2 and 3, figures 3 and 4). The greatest improvement in terms of speed was obtained by combining the two acceleration methods.